ACS APPLIED MATERIALS & INTERFACES

Research Article

www.acsami.org

Increase in the Water Contact Angle of Composite Film Surfaces Caused by the Assembly of Hydrophilic Nanocellulose Fibrils and Nanoclay Platelets

Chun-Nan Wu, Tsuguyuki Saito, Quanling Yang, Hayaka Fukuzumi, and Akira Isogai*

Department of Biomaterials Science, Graduate School of Agricultural and Life Sciences, The University of Tokyo, Tokyo 113-8657, Japan

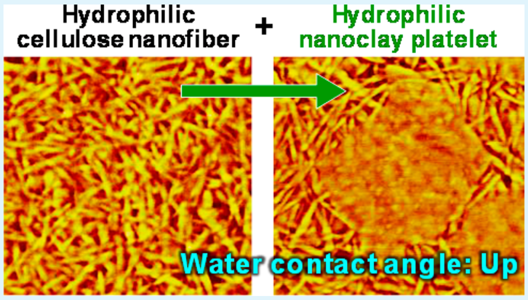

ABSTRACT: Controlling the assembly modes of different crystalline nanoparticles in composites is important for the expression of specific characteristics of the assembled structures. We report a unique procedure for increasing water contact angles (CAs) of composite film surfaces via the assembly of two different hydrophilic components, nanocellulose fibrils and nanoclay platelets. The nanocellulose fibrils and nanoclay platelets used have ionic groups on their surfaces in high densities (~1 mmol g^{-1}) and have no hydrophobic surface. The increase in the CA of the nanocellulose/nanoclay composite films was thus analyzed on the basis of the air area fractions of their nanostructured surfaces following Cassie's law. The air area fractions were geographically estimated from the atomic force microscopy height profiles of the composite film surfaces. The CAs of the composite film surfaces were found to be well described by Cassie's law. Interestingly, the composite films consisting of two hydrophilic nanoelements with different shapes exhibited CAs larger than those of the individual neat films.

KEYWORDS: *nanoclay, nanocomposite, surface roughness, TEMPO-oxidized cellulose nanofibril, water contact angle*

INTRODUCTION

Structurally new composite materials composed of nanofibrillar cellulose networks and layered silicate nanoparticles have recently been reported.[1−7] Such cellulose/silicate nanocomposites are nanoparticle assemblies and have a structure inherently different from that of conventional polymer/layered silicate (PLS) composites.[8] The silicate nanoplatelets within cellulose/silicate nanocomposites are in-plane oriented and form closely packed layered structures with the nanofibrillar cellulose. These nanocomposites form transparent and flexible films and have low densities of ~2 g cm^{-3} yet exhibit a very high strength of >500 MPa.[3,5,6] Furthermore, the cellulose/silicate nanocomposites show fire retardancy and gas barrier functions.[1]

Both cellulose and silicate are abundantly present in nature. Nanofibrillar cellulose can be prepared from bleached wood pulps for paper making by mechanical disintegration in water, which often includes chemical pretreatment of the pulp such as enzymatic hydrolysis,[9] carboxymethylation,[10] and 2,2,6,6-tetramethylpiperidinyl-1-oxyl (TEMPO)-mediated oxidation.[11,12] The resulting cellulose nanofibrils have widths and lengths of approximately 3−20 nm and 1−2 μm, respectively. Layered silicates are found in natural clay minerals, which are categorized into the following five groups on the basis of their chemical compositions and higher-order structures: smectite, illite, vermiculite, kaolinite, and chlorite.[13] Representative layered silicates used in the industrial field are montmorillonite (MTM) and saponite (SPN), both of which belong to the smectite group. While the platelet size of MTM (~300 nm) is much greater than that of SPN (~50 nm), both MTM and SPN nanoplatelets are approximately 1 nm thick.

The water contact angle (CA) is a parameter used to evaluate relationships between solid surfaces and water. When a solid surface is wetted with a water droplet, the droplet competes with the surrounding air to occupy a larger contact area with the solid surface.[14] The whole system then reaches an equilibrium state, and the CA between the solid−liquid and liquid−gas interfaces can be observed. The CA is governed by the chemical composition and topology of the solid surface.[14,15] A large CA indicates that the solid surface has a low surface energy or a high hydrophobicity. A common approach used to increase CAs is chemical modification of the solid surface with hydrophobic compounds such as alkyl ketene dimer (AKD).[12,16] Another approach is increasing the roughness of the surface; rough surfaces contain air with a CA of 180°, and these air fractions can play a role in propping up a water droplet from the surface.[17] In fact, the hydrophobicity of a material can be controlled by its surface morphology. It has been reported that the CA of a lauric acid film increased from 75° to 178° when nanoscale pins perpendicular to the film surface were fabricated on it.[18] Although these nanopins were covered with lauric acid and were thus chemically hydrophilic, the patterned surface contained an extremely high air fraction of 99%, resulting in the induction of a very high hydrophobicity.

Received: May 3, 2014
Accepted: June 30, 2014
Published: June 30, 2014

dx.doi.org/10.1021/am502701e | *ACS Appl. Mater. Interfaces* 2014, 6, 12707−12712

Here we report a unique procedure for increasing the CA of nanofibrillar cellulose/layered silicate nanocomposite film surfaces. The nanofibrillar cellulose used in this study was prepared from wood cellulose via TEMPO-mediated oxidation.[11,12] For the layered silicate, we used MTM and SPN clay nanoplatelets, which have different aspect ratios. Not only the TEMPO-oxidized cellulose nanofibrils (TOCNs) but also MTM and SPN nanoplatelets have anionic groups on their surfaces at a high density ($\sim$1 mmol g^{-1}) and have no hydrophobic surfaces. However, the CAs of the TOCN/MTM and TOCN/SPN composite films are significantly larger than those of neat TOCN, MTM, or SPN films. In this study, this astonishing phenomenon was thus analyzed on the basis of the air area fraction of the composite surfaces, following Cassie's law. Cassie's law has been used to interpret CAs in terms of various structures of material surfaces, and its applicability or limitation has been reported in detail by Gao and McCarthy.[19]

■ EXPERIMENTAL SECTION

Materials. A softwood bleached kraft pulp with a water content of 80% was supplied by Nippon Paper Industries (Tokyo, Japan). The hemicelluloses and residual lignin contents of the pulp are $\sim$10 and <0.1%, respectively, according to the data from the manufacturer. The viscosity average degree of polymerization of the pulp was 1270, measured using 0.5 M copper ethylenediamine.[20,21] The pulp had been kept in a wet state after the bleaching treatment and was subjected to a TEMPO oxidation reaction without drying. MTM and SPN powders were supplied by Kunimine Industries (Tokyo, Japan). The negative charge densities of MTM and SPN nanoplatelets were 0.7 and 0.9 mmol g^{-1}, respectively, which were measured using the conductivity titration method.[22] All other chemicals were purchased from Wako Pure Industries (Osaka, Japan) and used as received.

TOCN Dispersion. The TEMPO oxidation reaction was conducted on the bleached softwood pulp according to a previously reported method.[6] The carboxylate content of the TEMPO-oxidized pulp was 1.2 mmol g^{-1}, which was determined using the conductivity titration method.[22] The TEMPO-oxidized pulp was suspended in water (150 mL) at a concentration of 0.11% (w/v) and treated with a double-cylinder-type homogenizer (Physcotron NS-56, Microtec, Tokyo, Japan) at 7500 rpm for 1 min and then with an ultrasonic homogenizer equipped with a 26 mm probe tip (US300T, Nihon Seiki, Tokyo, Japan) operating at an output power of 210 W for 4 min. The unfibrillated fraction (<10%) was removed by centrifugation at 12000*g* for 20 min, and the supernatant was used as a TOCN dispersion [$\sim$0.1% (w/v)]. The width and length of the TOCN thus prepared were $\sim$4 nm and 1.1 ± 0.4 μm, respectively, which were measured from transmission electron microscopy (TEM) images of 150 isolated TOCN elements using image processing software.[23]

Silicate Nanoplatelet Dispersion. MTM or SPN powder (0.6 g) was added to distilled water (30 mL) in small increments while the mixture was stirred for 1 h. The resulting 2% (w/v) suspension was treated with the double-cylinder-type homogenizer at 7500 rpm for 1 min and then with the ultrasonic homogenizer equipped with a 7 mm probe tip operating at an output power of $\sim$10 W for 4 min. The silicate nanoplatelet dispersions thus obtained were stable and exhibited no sedimentation by visual inspection after 1 day.

TOCN/Silicate Nanoplatelet Composites. TOCN/silicate nanoplatelet composite films were prepared according to a previously reported method.[6] The 2% (w/v) dispersion of MTM or SPN nanoplatelets (0.015−1.5 mL) was added to the 0.1% (w/v) TOCN dispersion (30 mL) while the mixture was stirred for 1 h. The mixed dispersion was poured into a polystyrene Petri dish that was 50 mm in diameter and oven-dried at 40 °C for 3 days. The TOCN/silicate nanoplatelet composite film formed on the dish was peeled off and conditioned at 23 °C and 50% relative humidity (RH) for 1 day. The TOCN/MTM composite films with TOCN:MTM weight ratios of 99:1, 95:5, 90:10, 75:25, and 50:50 were termed TM01, TM05, TM10, TM25, and TM50, respectively. The TOCN/SPN composite films were similarly termed TS01, TS05, TS10, TS25, and TS50, respectively.

Analyses. The CAs of 2 μL water droplets on the film surfaces originally attached to the Petri dishes in the film preparation were measured five times for different parts of each film at 23 °C and 50% RH using a FAMAS DM500 apparatus (Kyowa Interface Science). The morphologies of the dispersed silicate nanoplatelets and the composite film surfaces were analyzed by atomic force microscopy (AFM) in air using a Nanoscope IIIa (Veeco Instruments) equipped with a silicon nitride cantilever tip in tapping mode. The height and phase images of the silicate nanoplatelets were taken on flat mica surfaces; a 0.001% (w/v) silicate nanoplatelet dispersion (5 μL) was dropped onto a freshly cleaved surface of mica (1 cm × 1 cm) and vacuum-dried at 60 °C for 48 h before observation. Both the thicknesses and lateral sizes of the nanoplatelets lying on the flat mica surface were determined from the AFM height profiles of 135 nanoplatelets. The aspect ratios of the nanoplatelets were calculated from the thicknesses and lateral sizes. Each MTM nanoplatelet having an irregular circumference shape was regarded as a circle using image processing software, and the circle diameter was used as the lateral MTM size for the aspect ratio calculation. The height and phase images of the film surfaces were taken from areas of 1 μm × 1 μm and 14 μm × 14 μm, respectively. The root-mean-square roughness (R_q) and power spectral densities of the film surfaces were calculated from the height profiles. The area fractions of the air on the film surfaces were geographically calculated using the bearing analysis function of the AFM software.[24,25]

■ RESULTS AND DISCUSSION

Morphology of Silicate Nanoplatelets. Figure 1 shows AFM images of the MTM and SPN nanoplatelets used in this study. The average thicknesses of both the MTM and SPN nanoplatelets were 1.1 nm, suggesting that both types of nanoplatelets were exfoliated to individual elements in the water dispersions. The MTM nanoplatelets are irregular in shape and have sharp edges. In contrast, SPN nanoplatelets are somewhat circular and are very small and homogeneous in size. The aspect ratios of the MTM and SPN nanoplatelets were 281 ± 97 and 47 ± 7, respectively (Figure 2; see the Experimental Section for the aspect ratio calculation).

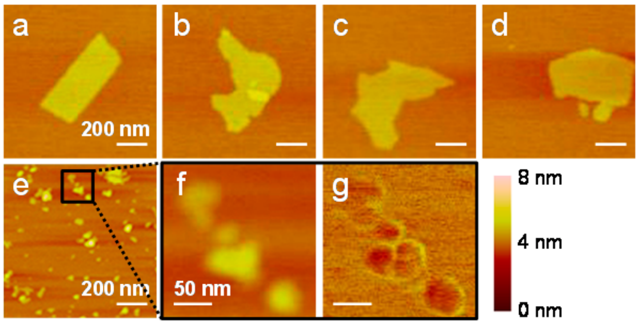

Figure 1. AFM height images of (a−d) MTM and (e and f) SPN nanoplatelets. Image f is a high-magnification image of the square part in image e. (g) Phase image of image f.

Water Contact Angle. Figure 3 shows the CAs of the TOCN/MTM and TOCN/SPN composite film surfaces that faced the Petri dish during the film preparation. The CAs of these composites were larger than those of the neat TOCN and the neat silicate films. The CAs of the composites increased as the silicate content was increased from 1 to 50% (w/w) [0.5 to 35% (v/v)]. These results show that the surfaces of the neat TOCN and neat silicate films became more apolar after the incorporation of the silicate nanoplatelets. However, all the

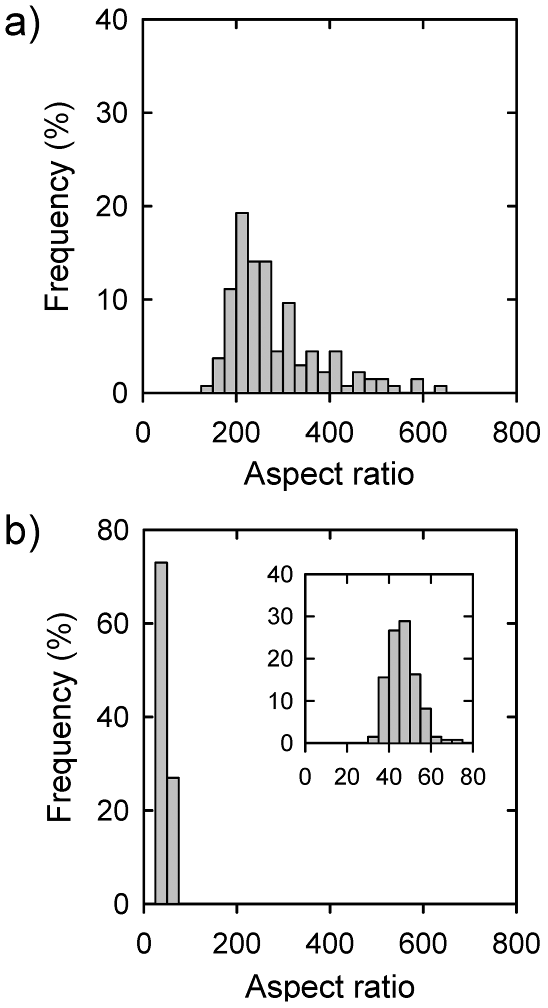

Figure 2. Aspect ratio distributions of (a) MTM and (b) SPN nanoplatelets.

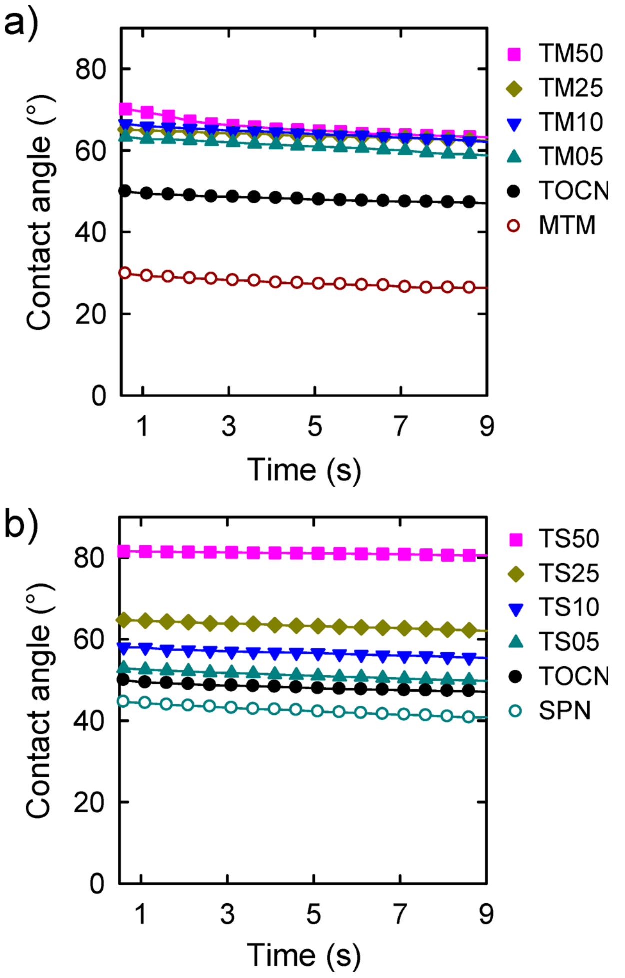

Figure 3. (a) CAs of the neat TOCN, TOCN/MTM, and neat MTM film surfaces. (b) CAs of the neat TOCN, TOCN/SPN, and neat SPN film surfaces.

elements in the composites, i.e., the TOCNs and silicate nanoplatelets, have hydrophilic ionic groups and no hydrophobic surface. Thus, the observed increase in the CA of the composites should be explained in terms of surface roughness and/or some mechanisms other than the chemical structures of their elements. Similar results were obtained for the composite film surfaces opposite to those facing the Petri dish during the film preparation, but the CA values fluctuated much more, probably because of the greater roughness of these film surfaces. We have previously reported that both the MTM and SPN nanoplatelets were homogeneously distributed in the film thickness direction of the composites.[5,6]

Surface Roughness. Figure 4 shows AFM images of the TOCN, TM50, and TS50 film surfaces. Nanofibrillar structures were clearly observed in both the height and phase images of the TOCN film (Figure 4a,d). For the TM50 and TS50 composite films, the grain boundaries of TOCNs and silicate nanoplatelets were obscure in the height images (Figure 4b,c), but they are clearly identifiable in the phase images (Figure 4e,f). Phase images are a helpful tool for identifying surface elements that are difficult to observe in height images,[26] although phase images are also reflected by topological heterogeneity based on the stiffness of the material surface and adhesion force between the cantilever tip and material surface. The sizes of the MTM and SPN nanoplatelets in the phase images of the composite surfaces correspond well to the lateral sizes measured for the individual silicate nanoplatelets dispersed on flat mica surfaces (Figure 1), suggesting that the silicate nanoplatelets were in-plane oriented on the film surfaces.

The root-mean-square roughness (R_q) and spatial wavelengths were calculated from the AFM height profiles for 14 μm × 14 μm surface areas (Figure 5 and Table 1). Both TOCN/MTM and TOCN/SPN composites had R_q values higher than and spatial wavelengths longer than those of the neat TOCN film. The TOCN/MTM composites had R_q values higher than and spatial wavelengths longer than those of the TOCN/SPN composites. R_q is a parameter that quantifies the surface roughness of materials.[27,28] A high R_q value means a sharp change in height in the vertical direction on the material surface. However, R_q is unable to indicate a change in height in the horizontal direction such as the distance between two adjacent hills. The spatial wavelengths, which are calculated from the power spectral densities of the height images, show the change in height in the horizontal direction.[27,28]

Relationship between the Contact Angle and Surface Roughness. As shown in Figure 5, the CAs measured correlated to the R_q values and spatial wavelengths of the composites; the CA increased with R_q and with spatial wavelength. However, the increases in CA were not explained

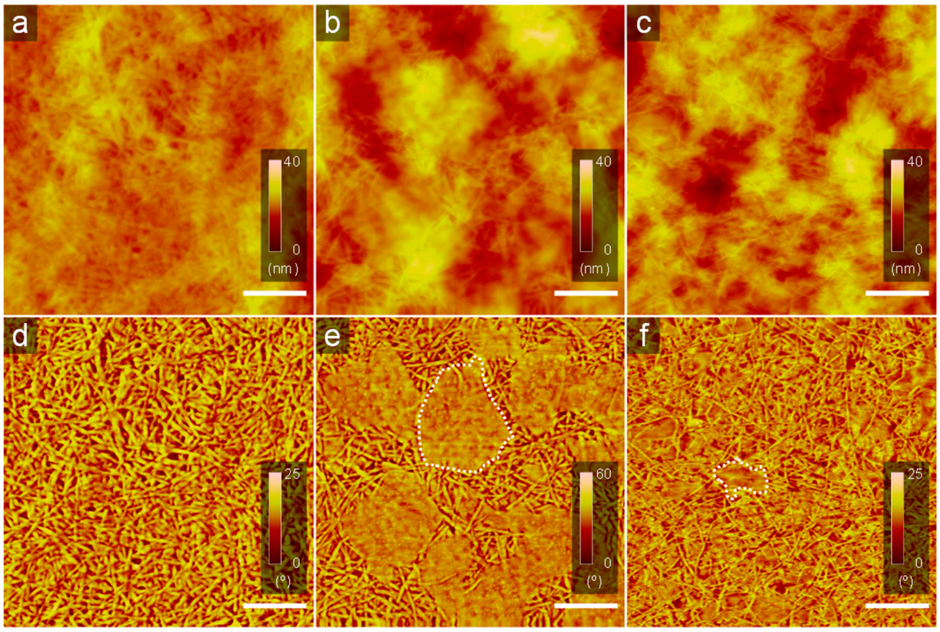

Figure 4. AFM height images and phase images of the surfaces of (a and d) TOCN, (b and e) TM50, and (c and f) TS50 films. The scale bars are 200 nm. The dashed lines in images e and f outline MTM and SPN nanoplatelets located on the surfaces, respectively.

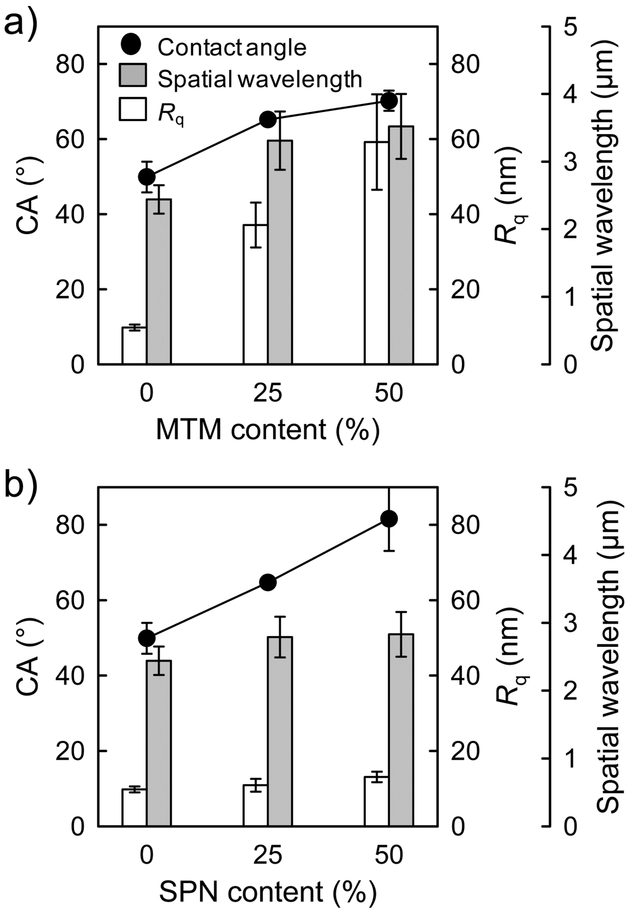

Figure 5. R_q values, CAs, and spatial wavelengths of the (a) TOCN/MTM and (b) TOCN/SPN composite film surfaces.

Table 1. CAs, R_q Values, Spatial Wavelengths, and Air Area Fractions of the Neat TOCN, TOCN/MTM, and TOCN/SPN Composite Surfaces

sample	CA (deg)	R_q (nm)	spatial wavelength (μm)	air area fraction (%)
TOCN	50 ± 4	10 ± 1	2.4 ± 0.2	18 ± 3
TM25	65 ± 1	37 ± 6	3.3 ± 0.4	31 ± 10
TM50	70 ± 3	59 ± 13	3.5 ± 0.5	33 ± 8
TS25	65 ± 1	11 ± 2	2.8 ± 0.3	28 ± 5
TS50	82 ± 9	13 ± 1	2.8 ± 0.3	38 ± 5

solely by the R_q value or spatial wavelength (Figure 6). The correlation coefficients, or r^2 values, between the CAs and the R_q values or spatial wavelengths were very low (0.2–0.4). Thus, the air fractions on the nanostructured surfaces should be taken into account in explaining this phenomenon.[18] Cassie's law is often used to explain the CAs of solid surfaces:

$$\cos\theta_c = f_1\cos\theta_1 + f_2\cos\theta_2 \tag{1}$$

where θ_c is the CA of the solid surface, θ_1 and θ_2 are the CAs of ideally flat surfaces of elements 1 and 2, respectively, f_1 and f_2 are the area fractions of elements 1 and 2 on the solid surface, respectively, and $f_1 + f_2 = 1$.[29] When element 2 is air, eq 1 is simplified by substituting an air CA of 180° for θ_2 as follows

$$\cos\theta_c = \cos\theta_1 - f_{air}(\cos\theta_1 + 1) \tag{2}$$

where f_{air} is the area fraction of air on the solid surface. Furthermore, when the solid element is ideally hydrophilic, $\theta_1 = 0$, resulting in the following equation

$$\cos\theta_c = 1 - 2f_{air} \tag{3}$$

In this study, all the elements within the composites, the TOCNs and silicate nanoplatelets, were covered with ionic groups and had no hydrophobic surfaces. Thus, the CA values for homogeneous composite surfaces can be estimated using eq 3. Cassie's law is valid when the chemical and morphological structures of the surface under a water droplet are identical to those at the three-phase contact line or the CA measuring point.[19]

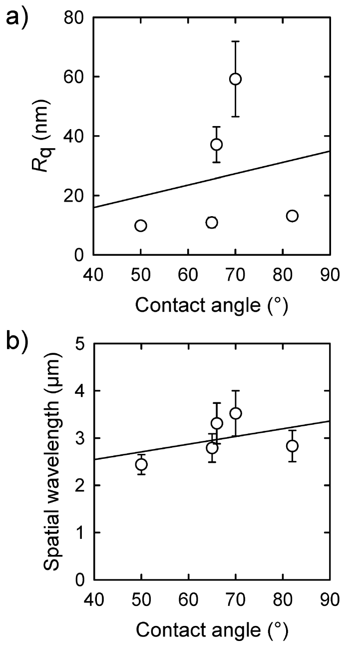

Figure 6. Relationship between the CAs and (a) R_q values and (b) spatial wavelengths of the TOCN/silicate nanoplatelet composite surfaces. The solid lines show the least-squares approximation between the CA and either R_q or spatial wavelength.

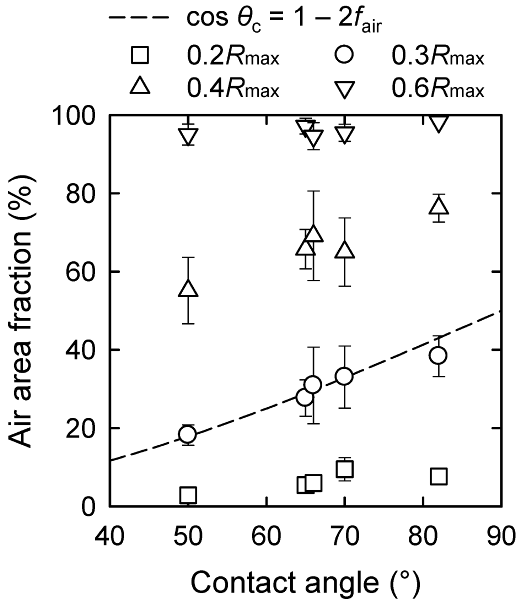

Figure 7. Relationship between the CA and air area fraction on the TOCN/silicate nanoplatelet composite surfaces. The air area fractions were estimated at different bearing heights ($0.2-0.6R_{max}$). The dashed line shows the relationship described by eq 3.

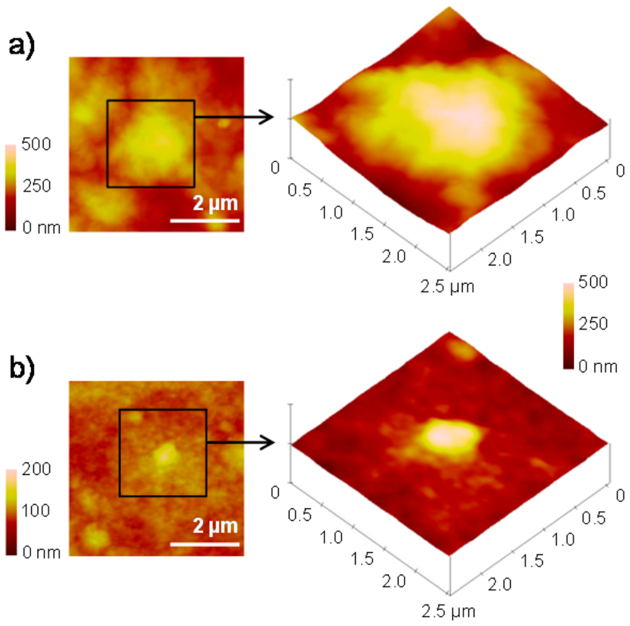

Figure 8. Three-dimensional AFM height images of the (a) TM50 and (b) TS50 film surfaces.

The area fractions of air on the film surfaces (f_{air}) were geographically calculated from their height profiles using the bearing analysis function of the AFM software (Table 1).[24,25] The height from the lowest position of the nanostructured surface to a certain height on the film surface is defined as the bearing height. The air area fraction is thus a function of the bearing height and increases with bearing height. The real height of the air fraction between a water droplet and the nanostructured surface is unmeasurable. Hence, height values z_i obtained by subtracting the height profiles of the nanostructured surface from the bearing height are assumed to be the heights of the air fraction under the water droplet. When height value z_i at a position is positive, the position is recognized as the air fraction in the bearing analysis.

Figure 7 shows the relationship between the CA and air area fraction assuming that the bearing height of the film is $0.3R_{max}$. The R_{max} value is the difference between the highest and the lowest positions of the nanostructured surface. The dashed line in this figure shows the theoretical relationship described by eq 3. The best fitting of the air area fractions of the composites to the theoretical line was observed when the bearing height was $0.3R_{max}$. This result indicates that the average height from the lowest position of the composite surfaces to the water droplets was $\sim 0.3R_{max}$. The CA values had a very good correlation with the air area fractions compared with their correlation with R_q values or spatial wavelengths (see Figure 6) and almost linearly increased with air area fraction.

It is noteworthy that the TS50 film showed an R_q value lower than and a spatial wavelength shorter than yet an air area fraction larger than those of the TM50 film. This phenomenon is probably related to the sizes of the silicate nanoplatelets on the composite surfaces. Figure 8 shows three-dimensional AFM height images of the TM50 and TS50 film surfaces. The high-aspect ratio MTM nanoplatelets formed large hills on the TM50 film surface. In contrast, the low-aspect ratio SPN nanoplatelets formed small hills on the TS50 film surface, which likely gave an R_q value lower than, a spatial wavelength shorter than, and an air area fraction larger than those of the TM50 film.

CONCLUSIONS

The water CAs on the cellulose/silicate composite films were larger than those of neat cellulose and neat silicate films and increased with the volume fraction of silicate in the composites from 0.5 to 35%. The surfaces of the cellulose nanofibrils and silicate nanoplatelets used in this study were covered with ionic groups at a high density (~1 mmol g^{-1}). Hence, the increase in the CA of the films was interpreted on the basis of the air area fraction of the nanostructured composite surfaces following Cassie's law. The CA values of the neat cellulose and cellulose/silicate composite films had a very good correlation with the air area fractions on their surfaces and were not described solely by the root-mean-square roughness or spatial wavelength of the surfaces.

■ AUTHOR INFORMATION

Corresponding Author

*E-mail: aisogai@mail.ecc.u-tokyo.ac.jp.

Notes

The authors declare no competing financial interest.

■ ACKNOWLEDGMENTS

This research was supported by Core Research for Evolutional Science and Technology (CREST) of the Japan Science and Technology Agency (JST).

■ REFERENCES

(1) Liu, A.; Walther, A.; Ikkala, O.; Belova, L.; Berglund, L. A. Clay Nanopaper with Tough Cellulose Nanofiber Matrix for Fire Retardancy and Gas Barrier Functions. *Biomacromolecules* **2011**, *12*, 633−641.

(2) Aulin, C.; Salazar-Alvarez, G.; Lindström, T. High Strength, Flexible and Transparent Nanofibrillated Cellulose−Nanoclay Biohybrid Films with Tunable Oxygen and Water Vapor Permeability. *Nanoscale* **2012**, *4*, 6622−6628.

(3) Ho, T. T. T.; Zimmermann, T.; Ohr, S.; Caseri, W. R. Composites of Cationic Nanofibrillated Cellulose and Layered Silicates: Water Vapor Barrier and Mechanical Properties. *ACS Appl. Mater. Interfaces* **2012**, *4*, 4832−4840.

(4) Sehaqui, H.; Kochumalayil, J.; Liu, A.; Zimmermann, T.; Berglund, L. A. Multifunctional Nanoclay Hybrids of High Toughness, Thermal, and Barrier Performances. *ACS Appl. Mater. Interfaces* **2013**, *5*, 7613−7620.

(5) Wu, C.-N.; Saito, T.; Fujisawa, S.; Fukuzumi, H.; Isogai, A. Ultrastrong and High Gas-Barrier Nanocellulose/Clay Layered Composites. *Biomacromolecules* **2012**, *13*, 1927−1932.

(6) Wu, C.-N.; Yang, Q.; Takeuchi, M.; Saito, T.; Isogai, A. Highly Tough and Transparent Layered Composites of Nanocellulose and Synthetic Silicate. *Nanoscale* **2014**, *6*, 392−399.

(7) Wang, J.; Cheng, Q.; Lin, L.; Jiang, L. Synergistic Toughening of Bioinspired Poly(vinyl alcohol)-Clay-Nanofibrillar Cellulose Artificial Nacre. *ACS Nano* **2014**, *8*, 2739−2745.

(8) Paul, D. R.; Robeson, L. M. Polymer Nanotechnology: Nanocomposites. *Polymer* **2008**, *49*, 3187−3204.

(9) Henriksson, M.; Henriksson, G.; Berglund, L. A.; Lindström, T. An Environmentally Friendly Method for Enzyme-Assisted Preparation of Microfibrillated Cellulose (MFC) Nanofibers. *Eur. Polym. J.* **2007**, *43*, 3434−3441.

(10) Wågberg, L.; Decher, G.; Norgren, M.; Lindström, T.; Ankerfors, M.; Axnäs, K. The Build-Up of Polyelectrolyte Multilayers of Microfibrillated Cellulose and Cationic Polyelectrolytes. *Langmuir* **2008**, *24*, 784−795.

(11) Saito, T.; Nishiyama, Y.; Putaux, J.-L.; Vignon, M.; Isogai, A. Homogeneous Suspensions of Individualized Microfibrils from TEMPO-Catalyzed Oxidation of Native Cellulose. *Biomacromolecules* **2006**, *7*, 1687−1691.

(12) Isogai, A.; Saito, T.; Fukuzumi, H. TEMPO-Oxidized Cellulose Nanofibers. *Nanoscale* **2011**, *3*, 71−85.

(13) Sposito, G. *The Chemistry of Soils*; Oxford University Press: New York, 1989.

(14) Marmur, A. Superhydrophobic and Superhygrophobic Surfaces: From Understanding Non-Wettability to Design Considerations. *Soft Matter* **2013**, *9*, 7900−7904.

(15) Feng, L.; Li, S.; Li, Y.; Li, H.; Zhang, L.; Zhai, J.; Song, Y.; Liu, B.; Jiang, L.; Zhu, D. Super-Hydrophobic Surfaces: From Natural to Artificial. *Adv. Mater.* **2002**, *14*, 1857−1860.

(16) Yang, Q.; Saito, T.; Isogai, A. Facile Fabrication of Transparent Cellulose Films with High Water Repellency and Gas Barrier Properties. *Cellulose* **2012**, *19*, 1913−1921.

(17) Laird, E. D.; Bose, R. K.; Qi, H.; Lau, K. K. S.; Li, C. Y. Electric Field-Induced, Reversible Lotus-to-Rose Transition in Nanohybrid Shish Kebab Paper with Hierarchical Roughness. *ACS Appl. Mater. Interfaces* **2013**, *5*, 12089−12098.

(18) Hosono, E.; Fujihara, S.; Honma, I.; Zhou, H. Superhydrophobic Perpendicular Nanopin Film by the Bottom-Up Process. *J. Am. Chem. Soc.* **2005**, *127*, 13458−13459.

(19) Gao, L.; McCarthy, T. J. How Wenzel and Cassie Were Wrong. *Langmuir* **2007**, *23*, 3762−3765.

(20) Shinoda, R.; Saito, T.; Okita, Y.; Isogai, A. Relationship between Length and Degree of Polymerization of TEMPO-Oxidized Cellulose Nanofibrils. *Biomacromolecules* **2012**, *13*, 842−849.

(21) Hiraoki, R.; Fukuzumi, H.; Ono, Y.; Saito, T.; Isogai, A. SEC-MALLS Analysis of TEMPO-Oxidized Celluloses using Methylation of Carboxyl Groups. *Cellulose* **2014**, *21*, 164−176.

(22) Saito, T.; Isogai, A. TEMPO-Mediated Oxidation of Native Cellulose. The Effect of Oxidation Conditions on Chemical and Crystal Structures of the Water-Insoluble Fractions. *Biomacromolecules* **2004**, *5*, 1983−1989.

(23) Fujisawa, S.; Ikeuchi, T.; Takeuchi, M.; Saito, T.; Isogai, A. Superior Reinforcement Effect of TEMPO-Oxidized Cellulose Nanofibrils in Polystyrene Matrix: Optical, Thermal, and Mechanical Studies. *Biomacromolecules* **2012**, *13*, 2188−2194.

(24) Mardilovich, A.; Kokkoli, E. Patterned Biomimetic Membranes: Effect of Concentration and pH. *Langmuir* **2005**, *21*, 7468−7475.

(25) Harris, M.; Appel, G.; Ade, H. Surface Morphology of Annealed Polystyrene and Poly(methyl methacrylate) Thin Film Blends and Bilayers. *Macromolecules* **2003**, *36*, 3307−3314.

(26) Schmitz, I.; Schreiner, M.; Friedbacher, G.; Grasserbauer, M. Phase Imaging as an Extension to Tapping Mode AFM for the Identification of Material Properties on Humidity-Sensitive Surfaces. *Appl. Surf. Sci.* **1997**, *115*, 190−198.

(27) Gavrila, R.; Dinescu, A.; Mardare, D. A Power Spectral Density Study of Thin Films Morphology Based on AFM Profiling. *Romanian Journal of Information Science and Technology* **2007**, *10*, 291−300.

(28) Duparré, A.; Ferre-Borrull, J.; Gliech, S.; Notni, G.; Steinert, J.; Bennett, J. M. Surface Characterization Techniques for Determining the Root-Mean-Square Roughness and Power Spectral Densities of Optical Components. *Appl. Opt.* **2002**, *41*, 154−171.

(29) Cassie, A. B. D.; Baxter, S. Wettability of Porous Surfaces. *Trans. Faraday Soc.* **1944**, *40*, 546−561.